Parametrization of homogeneous forested areas and effect on simulated dose rates near a nuclear research reactor[☆]

Gunther Bijloos [a,b,*], Johan Camps [a], Lise Tubex [a,1], Johan Meyers [b]

[a] SCK CEN, Belgian Nuclear Research Centre, Boeretang 200, BE-2400, Mol, Belgium
[b] Department of Mechanical Engineering, KU Leuven, Celestijnenlaan 300, BE-3001, Leuven, Belgium

ARTICLE INFO

ABSTRACT

One of the major uncertainties in dispersion-based simulations at the local scale is the representation of terrain effects. The aim of the current study is to quantify this type of uncertainty for dose-rate predictions over a homogeneous forest cover. At the Belgian reactor BR1, situated in a forested environment, ambient gamma-dose-rate data from routine Ar-41 releases are available in the first 300 m from the release point. We develop a forest parameterization that meets the site-specific needs, and integrate it in different dispersion models. Using different terrain-roughness parameterizations, we compare three types of models: a dispersion model driven by a Langevin equation, an advection-diffusion model, and a Gaussian plume model as a special case of the latter one. We find that all models are biased up to a factor of four, partly due to an uncertain source strength. The dose-rate uncertainty due to the model choice is a factor of 2.2 for a stack release and a factor of 14 for a ground release.

1. Introduction

Atmospheric dispersion models (ADM) describe the transfer of pollutants under given meteorological conditions and release characteristics. Such models are an indispensable tool for conducting qualitative impact assessments of nuclear facilities. In such assessments, both the effects of releases under normal operation and in case of an emergency situation on public health are examined. A particularly interesting application of dispersion modeling is ambient dose-rate estimation. Since dose rates are easy to measure, they are usually the first available measurements in case of a nuclear accident. Nuclear facilities are often marked by a complex terrain structure consisting of buildings, water surfaces and various vegetation types. Several ADM exist, ranging from simple Gaussian models to highly complex Computational Fluid Dynamics (CFD) models. Model selection depends on a compromise that has to be made between accuracy and the time that is required to set up cases and perform calculations. Gaussian models are widely used because of their simplicity, but they are presumed to fail in the first kilometer around the source due to complex terrain configurations (Leelőssy et al., 2018).

Empirical laws are elementary building blocks to model effects of terrain roughness. However, studies that discuss the sensitivity of incorporating terrain effects into simulated dose rates remain few (Oza et al., 1999; Raza et al., 2001; Srinivas et al., 2009). None of these studies investigated the influence of the terrain cover parameterization on simulated dose rates. In the current study, we investigate the modeling of terrain roughness in dispersion simulations and dose-rate predictions in a forested area that is horizontally homogeneous. To this end, we set up a suite of models, that differ in the amount of detail with which the forest cover is represented, but also differ in the type of dispersion parametrization. This includes a Gaussian plume model with two open-field parameterizations (low and high terrain roughness), and two different Lagrangian particle models (both with open-field and forest parametrization). The Gaussian plume model simply uses increased surface roughness to parametrize forest, following the standard approach for these models. For both other models, we develop a more detailed canopy parametrization. This describes the wind field and the dispersion process above and inside the canopy, hereby taking a non-uniform leaf distribution over height and the sparsity of the vegetation cover into account. All the models are harmonized, i.e., the Gaussian and Lagrangian models have each a similar implementation, the parameterization of the Lagrangian models is such that they

reproduce the same internal variability, and the dose rates are calculated in the same way.

As a point of reference, an ambient dose-rate dataset is available for the SCK CEN site (see Fig. 1), situated in a forest environment, by means of the TELERAD early warning stations (Sonck et al., 2010). On this site, increased dose rate levels are picked up regularly due to Ar-41 stack releases during the routine operation of the Belgian Reactor 1 (BR1). The data spans 16 days in the first half of 2017 with 25 consecutive 10-min periods per day. In-situ weather data from a met (meteorological) mast are also available. We reproduce this dataset with our different simulation models, and evaluate performance using the measures proposed by Chang and Hanna (2004). Although not available in the dataset, we also perform a model comparison for a hypothetical ground-release scenario for the same meteorological data series.

In section 2, an extensive description of the models is given. In section 3, the simulation results are presented. This section also contains a validation and a sensitivity study of the canopy model. The validation study addresses the capabilities of the canopy model to describe the atmospheric properties of the vegetation canopy. In section 4 a discussion of the results can be found. Finally, section 5 concludes the paper.

2. Methodology

In order to simulate the dose rate resulting from the dispersion of radioactive pollutants, a pollutant dispersion model is necessary that provides the pollutant concentration $c(t, \mathbf{x})$ (cf. further below for details.)

Given the concentration field, and a detector/observer at location $\mathbf{x}' \in \mathbb{R}^3$, the dose rate $\dot{d}_\gamma$ [Gy/s] due to the gamma energy released per disintegration E_γ [MeV] can be calculated as (Thykier-Nielsen et al., 1995, 1999)

$$\dot{d}_\gamma(t, \mathbf{x}') = \frac{K_c \mu_{en} E_\gamma}{4\pi} \int_{\mathbb{R}^3} \frac{B(\mu r(\mathbf{x}))}{r(\mathbf{x})^2} e^{-\mu r(\mathbf{x})} c(t, \mathbf{x}) d\mathbf{x} \quad (2.1)$$

with $K_c = 1.6 \times 10^{-13}$ Gy kg/MeV a unit conversion factor, μ_{en} the energy absorption coefficient for air [m^2/kg], B the buildup factor, μ the linear attenuation coefficient in air [m^{-1}] and $r(\mathbf{x})$ the Euclidean distance [m] from $\mathbf{x} \in \mathbb{R}^3$ to $\mathbf{x}'$. More information about the application of the dose rate model and its parameter values can be found in Kenis et al. (2013).

2.1. Dispersion modeling

In the following, we assume that the released gas does not deposit. In particular, the formulation is not valid for the release of polydisperse particulates, but this type of releases are not considered in the current work. A classical approach to model dispersion of radioactive pollutants

is to solve an advection-diffusion equation

$$\frac{\partial c}{\partial t} + \nabla \cdot (\mathbf{u}c) = \nabla \cdot (K\nabla c) - \lambda c + S \quad (2.2)$$

with c the concentration field [Bq/m^3], $\mathbf{u} = (u, v, w)$ the mean wind speed vector [m/s], λ the radioactive decay constant [s^{-1}], $K(\mathbf{x}) = \text{diag}(K_x(\mathbf{x}), K_y(\mathbf{x}), K_z(\mathbf{x})) \in \mathbb{R}^{3 \times 3}$ the eddy diffusivity tensor [m^2/s] and S the source term [Bq/(m^{3}s)]. In the current work, we will consider steady point releases, so that $S(\mathbf{x}) = Q\delta(\mathbf{x} - \mathbf{x}_0)$, with $\mathbf{x}_0$ the source location. Moreover, $\lambda = 0s^{-1}$ is used, since we will only study the near-field range, for which decay can be neglected.

The main disadvantage of using (2.2) to solve for the concentration field is that the Boussinesq approximation (i.e. $-\langle \mathbf{u}'c' \rangle = K\nabla c$, where the prime denotes the turbulent component of the respective field and the operator $\langle \cdot \rangle$ is the time average over a sufficiently long time span such that $\langle \mathbf{u}' \rangle = \langle c' \rangle = 0$) underestimates the turbulent diffusivity, and it is not valid close to the source (e.g., see De Visscher, 2013, §5.11.5 p.117). This is also shown by Taylor's statistical turbulence theory [44]. According to this theory, the standard deviation of the position of pollutant particles is proportional to the travel time close to the source. Only after a sufficiently long travel time, it becomes proportional to the square root of travel time, as consistent to, e.g., molecular dispersion and the Boussinesq approximation.

In order to incorporate Taylor's theory, a Lagrangian modeling framework has to be used. We first start by introducing a Lagrangian modeling framework that is equivalent to solving (2.2). Let the stochastic process $(X_t)_{t>0}$ describe a Lagrangian particle trajectory, and consider following stochastic differential equation to generate such trajectories

$$d\mathbf{X}_t = (\mathbf{u}(\mathbf{X}_t) + \mathbf{u}'_p)dt, \quad t > 0, \quad (2.3)$$

with $\mathbf{u}'_p$ the particle velocity noise vector [m/s] (see below), and $\mathbf{u}(\mathbf{x})$ the background mean wind field. If we select

$$\mathbf{u}'_p dt = \nabla \cdot K(\mathbf{X}_t)dt + \sqrt{2K(\mathbf{X}_t)}d\mathbf{W}_t \quad (2.4)$$

with $(\mathbf{W}_t)_{t>0}$ the three-dimensional Wiener process, and we consider $p(t, \mathbf{x}|t', \mathbf{x}')$ the transition probability density function of the stochastic process (Gardiner, 1985), i.e. the probability that a particle is situated in an infinitesimal volume $d\mathbf{x}$ around location $\mathbf{x}$ at time t given an earlier position $(t', \mathbf{x}')$, with $t' \le t$, then it can be shown that (Lamb, 1984)

$$c(t, \mathbf{x}) = Q \int_0^t p(t, \mathbf{x}|\tau, \mathbf{x}_0)d\tau \quad (2.5)$$

corresponds to the solution of (2.2) (see, e.g., Tubex, 2018).

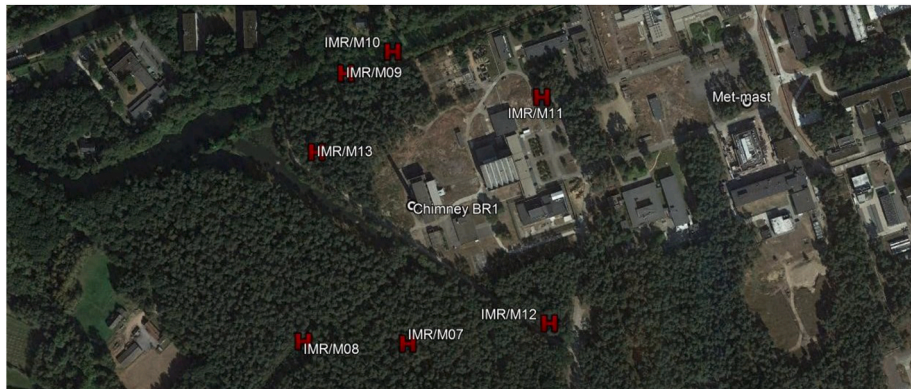In order to set up a Lagrangian framework that is consistent with

Fig. 1. The SCK CEN site, including the TELERAD monitoring stations (red marks), the chimney (or stack) and the met mast; image from Google Earth ©2017 Google. (For interpretation of the references to colour in this figure legend, the reader is referred to the Web version of this article.)

Taylor's theory, we use following Langevin equation for the k-th component of $\mathbf{u}'_p$ ($k = 1, 2, 3$) (Legg and Raupach, 1982)

$$d\left[\mathbf{u}'_p\right]_k = -\frac{\left[\mathbf{u}'_p\right]_k}{[\tau_L]_k}dt + \frac{\partial \sigma_w^2}{\partial z}dt\delta_{k3} + \left(\frac{2}{[\tau_L]_k}\right)^{1/2}[\sigma_{\mathbf{u}}]_k d[\mathbf{W}_t]_k \qquad (2.6)$$

with $\tau_L \in \mathbb{R}^3$ the Lagrangian time scale vector [s], $\sigma_{\mathbf{u}} = (\sigma_u, \sigma_v, \sigma_w) \in \mathbb{R}^3$ the variance vector [m/s] of the particle velocity and δ_{ij} the Kronecker delta. Here, the operator $[\cdot]_k$ returns the k-th component of the input vector.

Prior to solving (2.3), and (2.4) or (2.6), $\mathbf{u}$, K, $\sigma_{\mathbf{u}}$ and τ_L need to be determined. This requires a parametrization of the atmospheric conditions. In the current work, we presume homogeneous forested terrain, and therefore, we presume that profiles of velocity, turbulence intensities, etc. only depend on the vertical direction, viz. $\mathbf{u}(\mathbf{x}) = \overline{u}(z)\widehat{\mathbf{e}}$ with $\widehat{\mathbf{e}} \in \mathbb{R}^3$ the unit vector pointing along the horizontal wind direction and $\overline{u}(z)$ the velocity magnitude [m/s] at height z (see §2.2) for any point $\mathbf{x} \in \mathbb{R}^3$. Depending on possible further assumptions that we make, we arrive at four classes of models (an overview is given in Table 1), of which we will consider three in the current work. First of all, either using the Boussinesq hypothesis or Taylor's turbulence theory with a parametrization of the vertical profiles of velocity etc. leads to two models that we consider. However, often dispersion models are even more simplified by presuming also vertical homogeneity. In combination with the Boussinesq hypothesis, this allows to formulate an analytical solution to Eq. (2.2), leading to the well-known Gaussian plume model. Since this is a model that is widely used in dispersion studies, we include it here as well as a point of reference.

The aim of the current work is to evaluate the importance of a proper forest parametrization for dispersion simulations in homogeneous forested areas. To this end, we will use the Lagrangian models both with (*i*) an open-field parametrization and (*ii*) a forest parametrization. For the Lagrangian models, we construct terrain roughness models that provide vertical profiles of micro-meteorological conditions (see §2.2). If the open field or forest parameterization is substituted into Eq. (2.3), then the resulting model will be referred to as the OF (Open Field) or F (Forest) model respectively. In case the OF model is used, we employ a high terrain roughness that is representative of the total forest roughness. The Gaussian (G) plume models have been calibrated to tracer experiments or meteorological data (see §2.1.2 and §4). The terrain roughness for the Gaussian models is an intrinsic property of the scheme for the dispersion parameters and thus, it cannot be modified. We use two parameterizations i.e. the Pasquill–Gifford (PM) and the Bultynck–Malet (BM) scheme. In total, the different models and parameterizations lead to six different simulation models, as summarized in Table 2.

2.1.1. Lagrangian models: discretization

For the discretization of Eqs. (2.3), (2.4) and (2.6), we use the explicit Euler–Maruyama scheme. Given the initial condition $\mathbf{X}^0 = \mathbf{X}_0$, the discretized scheme is as follows for $n \geq 0$:

$$\mathbf{X}^{n+1} - \mathbf{X}^n = \left(\mathbf{u}(\mathbf{X}^n) + \mathbf{u}'^n_p\right)\Delta t, \qquad (2.7)$$

Table 1
Four possible model classes following from using the Boussinesq hypothesis or Taylor's turbulence theory, and from either assuming vertical homogeneity or not.

	Boussinesq hypothesis	Taylor's turbulence theory
Vertically homogeneous	Gaussian plume model (see §2.1.2)	–
Vertically non-homogeneous	Eqs. (2.3) & (2.4)	Eqs. (2.3) & (2.6)

$$\mathbf{u}'^n_p\Delta t = \nabla \cdot K(\mathbf{X}^n)\Delta t + \sqrt{2K(\mathbf{X}^n)}\Delta \mathbf{W}^{n+1}, \qquad (2.8)$$

$$\left[\mathbf{u}'^{n+1}_p\right]_k = \left(1 - \frac{\Delta t}{[\tau_L(\mathbf{X}^n)]_k}\right)\left[\mathbf{u}'^n_p\right]_k + \frac{\partial \sigma_w^2}{\partial z}(\mathbf{X}^n)\Delta t\delta_{k,3}$$
$$+ \left(\frac{2}{[\tau_L(\mathbf{X}^n)]_k}\right)^{1/2}[\sigma_{\mathbf{u}}(\mathbf{X}^n)]_k\Delta\left[\mathbf{W}^{n+1}_t\right]_k, \qquad (2.9)$$

in which the superscript n refers to the value at the n-th time step and the increment $\Delta[\mathbf{W}^{n+1}]_k$ is drawn from a normal distribution. For scheme (2.7,2.9), we assume $\mathbf{u}'^0_p$ to be the zero vector. Either combining (2.7) with (2.8), or (2.7) with (2.9), results in the discretization for the LB and LT models respectively.

The LT model (2.7,2.9) requires $\Delta t \leq 2\min_k[\tau_L]_k$ for the scheme to remain stable. For an accurate convergence, however, $\Delta t < \min_k[\tau_L]_k$ is highly recommended. The LB model (2.7,2.8) has no stability restrictions. From a physical perspective, this model presumes $\mathbf{u}'_p$ to be uncorrelated in successive time steps. This would require $\Delta t > \max_k[\tau_L]_k$, but this condition is not enforced in practice in the current work, as it would lead to particles that are spread out too thin in the domain of interest.

Model (2.7,2.9) differs fundamentally from (2.7,2.8) because it incorporates the inertia effect to which the pollutant particles are subjected. This effect is modeled by means of the air parcel's velocity autocorrelation that the particle is initially following. Model (2.7,2.8) does not take this inertia effect into account. The internally generated variance after one time step from both models, however, can be set equal. Denote $\sigma_k^{2,n} = \mathrm{Var}([\mathbf{u}'^n_p]_k(|\mathbf{X}^{n-1}))$, and assume $\tau_L(\mathbf{X}^n) = \tau_L(\mathbf{X}^0)$ and $\sigma_{\mathbf{u}}(\mathbf{X}^n) = \sigma_{\mathbf{u}}(\mathbf{X}^0)$. One can prove by induction from Eq. (2.9) the following identity

$$\sigma_k^{2,n} = \sigma_k^{2,0}\left(1 - \frac{\Delta t}{[\tau_L(\mathbf{X}^0)]_k}\right)^{2n} + \frac{2\Delta t}{[\tau_L(\mathbf{X}^0)]_k}[\sigma_{\mathbf{u}}(\mathbf{X}^0)]_k^2 \sum_{l=0}^{n-1}\left(1 - \frac{\Delta t}{[\tau_L(\mathbf{X}^0)]_k}\right)^{2l}.$$

Choose $T \in \mathbb{R}_0^+$ randomly, but fixed and set $\Delta t = T/m$ with $m \in \mathbb{N}_0$ sufficiently large such that $\Delta t < [\tau_L(\mathbf{X}^0)]_k$, then

$$\sigma_k^2(T) := \lim_{m\to\infty}\sigma_k^{2,m} = \sigma_k^{2,0}e^{-2T/[\tau_L(\mathbf{X}^0)]_k} + [\sigma_{\mathbf{u}}(\mathbf{X}^0)]_k^2\left(1 - e^{-2T/[\tau_L(\mathbf{X}^0)]_k}\right). \qquad (2.10)$$

The same expression was also derived in Legg and Raupach (1982). Assume that after n time steps, the values $\mathbf{u}'^n_p$ and $\mathbf{X}^n$ are obtained from Eqs. (2.7,2.9), consequently $\sigma_k^{2,n} = 0$ at the next time step and apply (2.10) with $T = \Delta t$, i.e.,

$$\sigma_k^{2,n+1} = [\sigma_{\mathbf{u}}(\mathbf{X}^n)]_k^2\left(1 - e^{-2\Delta t/[\tau_L(\mathbf{X}^n)]_k}\right). \qquad (2.11)$$

It can be readily seen that $\sigma_k^{2,n+1} = 2K(\mathbf{X}^n)/\Delta t$ in case of (2.7,2.8). Setting this expression equal to (2.11) yields

$$K_{k,k}(\mathbf{X}^n) = \frac{[\sigma_{\mathbf{u}}(\mathbf{X}^n)]_k^2}{2}\Delta t\left(1 - e^{-2\Delta t/[\tau_L(\mathbf{X}^n)]_k}\right). \qquad (2.12)$$

We will assume this form for the main diagonal elements of K to match the internally generated variability of both models for $\Delta t < \min_k[\tau_L]_k$. Consequently, possible simulation differences are not attributed to differences in variability.

Finally, the discretization of (2.1) is highly elaborated. Denote $f : \mathbb{R}^3 \to \mathbb{R}$ an integrable function, then the expectation value w.r.t. $(\mathbf{X}_t)_{t>0}$ generated by (2.3,2.4) or (2.3,2.6) is given by

$$\mathbb{E}[f(\mathbf{X}_{t-s})] = \int_{\mathbb{R}^3}f(\mathbf{x})p(t, \mathbf{x}|s, \mathbf{x}_0)d\mathbf{x}, \quad s < t, \; s \geq 0, \qquad (2.13)$$

with p the corresponding probability density function. Substituting (2.5) in (2.1), switching the order of integration and applying (2.13) at time

$t = t_n := n\Delta t$ yields

$$\dot{d}_\gamma(t_n, \mathbf{x}') = \frac{QK_c\mu_{en}E_\gamma}{4\pi} \int_0^{t_n} \mathbb{E}\left[\frac{B(\mu r(\mathbf{X}_{t_{n-s}}))}{r(\mathbf{X}_{t_{n-s}})^2} e^{-\mu r(\mathbf{x}_{t_{n-s}})}\right] ds.$$

Now, approximating the expectation value $\mathbb{E}[\cdot]$ by the arithmetic average and discretizing the integral over time results in the approximation

$$\dot{d}_\gamma(t_n, \mathbf{x}') \approx \frac{QK_c\mu_{en}E_\gamma}{4\pi N_p} \sum_{i=1}^n \sum_{j=1}^{N_p} \frac{B\left(\mu r\left(\mathbf{X}_j^{n-i}\right)\right)}{r\left(\mathbf{X}_j^{n-i}\right)^2} e^{-\mu r\left(\mathbf{x}_j^{n-i}\right)} \Delta t_i \quad (2.14)$$

with $\mathbf{X}_j^{n-i}$ the location at the n-th time step of the j-th particle released at the i-th time step and N_p the number of particles released per time step. Notice that Δt_i is the employed time step at the moment of release of the corresponding particle.

2.1.2. Gaussian plume model

Equation (2.2) has a well-known analytical solution for the setting of a homogeneous, stationary turbulence field. This assumption reduces the complexity of (2.2) greatly since it implies a uniform velocity over space. Given additional assumptions on the dispersion coefficient and boundary conditions, among others, following analytical solution can be

$$c(x, y, z) = \frac{Q}{2\pi u_e\sigma_y\sigma_z} \exp\left\{-\frac{1}{2}\left(\frac{y}{\sigma_y}\right)^2\right\} \left(\exp\left\{-\frac{1}{2}\left(\frac{z - h_e}{\sigma_z}\right)^2\right\} + \exp\left\{-\frac{1}{2}\left(\frac{z + h_e}{\sigma_z}\right)^2\right\}\right)$$

derived (Stockie, 2011)

with σ_y and σ_z the dispersion parameters [m], h_e the emission height [m], and u_e the wind speed [m/s] at height h_e. The following expressions relate the dispersion parameters to the eddy diffusivities (Stockie, 2011)

$$\frac{1}{2}\frac{d\sigma_y^2}{dx} = u_e^{-1}\int_0^x K_y(\xi)d\xi, \quad \frac{1}{2}\frac{d\sigma_z^2}{dx} = u_e^{-1}\int_0^x K_z(\xi)d\xi, \quad (2.15)$$

with x the downwind distance [m]. The literature provides several parameterization schemes, but in this paper we use the Pasquill–Gifford (Zannetti, 1990) (PG in Table 2), and the in-house scheme by Bultynck and Malet (1972) (BM in Table 2).

The Pasquill–Gifford scheme was derived from a tracer experiment in which ground releases took place in a low-roughness open field, and is used here for the G–PG simulation. The in-house scheme was calibrated to data from the met mast at the SCK CEN site to represent the different atmospheric conditions occurring at the site. Then, the obtained scheme was validated with tracer experiments. During these experiments, stack releases (60 m) took place in rough terrain, i.e. the SCK CEN site (Bultynck and Malet, 1972), and these terrain characteristics are used in the G–BM formulation. The Pasquill–Gifford and in-house schemes were originally derived for averaging times of 3 min and 1 h respectively. In this study, these schemes are used to simulate an averaging time of 10 min.

For the Pasquill–Gifford scheme u_e is estimated using Monin–Obhukov similarity theory (see also §2.2) with $z_0 = 0.03$m (low roughness, Wieringa, 1992). For the in-house scheme, a power-law fit $\overline{u}(z) = \overline{u}_{ref}[z/z_{ref}]^\alpha$ is used, with values for α provided in Table 3. It is important to emphasize that the stability class is a parameter in both schemes, but not the terrain roughness. The latter one is an intrinsic property of the scheme.

2.2. Atmospheric parameterization

Both (2.8) and (2.9) require profiles of vertical velocity, and turbulence statistics for different atmospheric conditions. Input is typically a measurement of wind speed, direction, and temperature at a reference height, obtained from a met mast. The terrain parameterizations are matched to these local measurements to represent the local micro-meteorological conditions. In the current work, we assume a reference measurement well above the forest canopy. Thus, the canopy parameterization extrapolates the meteorological conditions from above to inside the canopy. Moreover, we compare such a canopy model to a more conventional open-field model based on Monin–Obhukov similarity theory (see §2.2.1), using a high terrain roughness to represent the forest.

2.2.1. Open-field parametrization

The simplest way to represent a forest in the inhomogeneous turbulence case is by modeling it as an open field with high-terrain roughness. The Eulerian wind profile can be directly obtained from Monin–Obukhov similarity theory (MOST) (e.g., Arya, 2001), i.e.,

$$\overline{u}(z; u_*, L) = \frac{u_*}{\kappa}\left(\ln\left(\frac{z}{z_0}\right) - \Psi_M(z/L) + \Psi_M(z_0/L)\right) \quad (2.16)$$

with u_* the friction velocity [m/s], $\kappa = 0.4$ the Von Kármán constant [-], z_0 the roughness length [m], L the Monin-Obukhov length [m] and Ψ_M the integrated stability kernel. The virtual potential temperature [K] has a similar expression as (2.16), i.e., (Arya, 2001)

$$\theta_v(z; \theta_*, L) - \theta_{v,0} = \frac{\theta_*}{\kappa}\left(\ln\left(\frac{z}{z_{0,H}}\right) - \Psi_H(z/L) + \Psi_H\left(z_{0,H}/L\right)\right) \quad (2.17)$$

with $\theta_{v,0}$ the virtual potential temperature at height $z_{0,H}$ [m], and θ_* the temperature scale [K]. The stability functions from Dyer (1974) are used. The expressions for the integrated forms are given by (A.10-A.11) (e.g., see De Ridder, 2010).

The virtual potential temperature is simply related to temperature and humidity using the standard definitions (Holton, 2004),

$$\theta_v(z) = T_v(z)\left(\frac{p_0}{p(z)}\right)^{R/c_p}, \quad R = 287\,J/(kg\,K), \quad c_p = 1004J/(kg\,K),$$

$$(2.18)$$

Table 2
Overview of the different models and terrain parametrizations considered in the current study, including acronyms used in the text.

	Imposed roughness	Gaussian plume	Lagrangian + Boussinesq	Lagrangian + Taylor
Open field	low	G–PG	–	–
	high	G–BM	LB–OF	LT–OF
Forest	high	–	LB–F	LT–F

Table 3
Values of the exponent α for each stability class (Kretzschmar et al., 1984) as used in the in-house scheme.

	stable	slightly stable	neutral	slightly unstable	unstable	very unstable
α	0.53	0.40	0.33	0.23	0.16	0.10

$$T_v(z) = T(z)\frac{1 + r_v(T(z))/0.622}{1 + r_v(T(z))}, \quad r_v(z) = \frac{0.622e_v(T(z))}{p(z) - e_v(T(z))}, \quad e_v(z) = RH(z)e_s(T(z)),$$
(2.19)

presuming hydrostatic equilibrium for the pressure ($dp/dz = -\rho g$, using a density $\rho = 1.225$ kg/m^3, gravitational acceleration $g = 9.81$ m/s^2 and pressure at sea level $p_0 = 101300$ Pa), and with T the ambient temperature [K], r_v [$-$] the mixing ratio, e_v [Pa] the vapor pressure, RH [$-$] the relative humidity, and e_s [Pa] the saturation vapor pressure over water. The parameter e_s is calculated here using the Buck equation (A.15) (Buck, 1981).

Given measurements of velocity $\overline{u}_{\text{ref}}$ at height z_{ref}, virtual potential temperatures θ_{ref} at height $\overline{z}_{ref}$ and $\theta_{v,0}$ at height $z_{0,H}$, i.e.,

$$\overline{u}(z_{\text{ref}}; u_*, L) = \overline{u}_{\text{ref}}, \quad \theta_v(\overline{z}_{ref}; \theta_*, L) - \theta_{v,0} = \Delta\theta_{v,\text{ref}}, \quad L = \frac{u_*^2 \theta_{v,0}}{\kappa g \theta_*}.$$
(2.20)

We obtain a closed system of three equations that can be used to obtain L, u_*, and θ_*, as well as the height-dependent profiles. This profile-fixing strategy is the so-called profile method (Holtslag, 1984).

Apart from velocity profiles, also turbulence statistics are required. For Eq. (2.4), the same profiles for σ_u, σ_v, σ_w, and $[\tau_L]_k$ ($k = 1, 2, 3$) are used in the expression for K (2.12) as for Eq. (2.6). To this end, we presume that measured statistics of wind direction at reference height

$$[\tau_L]_3 = 0.15\frac{h_{\text{ABL}}}{\sigma_w}\left[1 - \exp\left(\frac{-5z}{h}\right)\right], \quad -200\text{m} < L < 0\text{m and } z > 0.1h_{\text{ABL}}.$$
(2.28)

The expression for τ_L in stable and unstable conditions requires the height of the boundary layer, h_{ABL}, as an input. In case of a stable atmosphere, the height is estimated as $h_{\text{ABL}} = 0.25\sqrt{u_*L/f_C}$ ($0\text{m} < L < 200\text{m}$) (Hanna, 1984) with f_C the Coriolis parameter. For unstable conditions ($-200\text{m} < L < 0\text{m}$):

$$h_{\text{ABL}} = \begin{cases} 2|L| \cdot \left([\sigma_v/u_*]^3 - 12\right) & , -200\text{m} < L < -100\text{m and } (\sigma_v/u_*)^3 > 12 \\ \theta_{v,0}(\sigma_v/0.6)^3\big/(-u_*\theta_*g) & , \text{otherwise} \end{cases}$$

The second equation is a good approximation in very unstable conditions (Caughey, 1984) (typically $-100\text{m} < L < 0\text{m}$), but we use it for a wider range of unstable conditions ($-200\text{m} < L < -100\text{m}$ when $(\sigma_v/u_*)^3 \leq 12$), as we did not find a better option.

2.2.2. Vegetation canopy dispersion model

In the current section, we introduce a new forest canopy model by combining elements from De Ridder (2010), Mihailović et al. (1999) and Yi (2008). These models are consistent with the classical log law higher up above the forest, take the sparsity of the forest into account, and

$$\sigma_u = 1.2\sigma_{v,r} \quad (|L| > 200\text{m}), \quad \sigma_u = 1.5\sigma_{v,r} \quad (0\text{m} < L < 200\text{m}), \quad \sigma_u = \sigma_{v,r} \quad (-200\text{m} < L < 0\text{m}).$$
(2.22)

are available, i.e. the standard deviations σ_{azi} [°] and σ_{elev} [°] of azimuth and elevation angles respectively. Using $w \approx 0$ m/s, and presuming small angles, we then find

$$\sigma_{v,r} \approx \overline{u}_{\text{ref}}\sigma_{\text{azi}}\frac{\pi}{180°}, \quad \sigma_{w,r} \approx \overline{u}_{\text{ref}}\sigma_{\text{elev}}\frac{\pi}{180°}.$$
(2.21)

In the surface layer, the variance of the horizontal wind components can be assumed to be independent of height for every stratification regime (e.g., see Stull, 1988; Hunt, 1984; Caughey, 1984), so that $\sigma_v(z) = \sigma_{v,r}$. The velocity variation along the wind direction, is parameterized as (Stull, 1988; Hanna, 1984)

The variance of the vertical wind component is also height independent, except in an unstable atmosphere. According to local free convection similarity theory $\sigma_w(z) = \sigma_{w,r}(z/z_{\text{ref}})^{1/3}$ (e.g., Arya, 2001).

The Lagrangian time scale τ_L is considered to be a three-dimensional vector; a parameterization for each component can be found in Hanna (1984) i.e.

$$[\tau_L]_1 = [\tau_L]_2 = [\tau_L]_3 = \frac{0.5z/\sigma_w}{1 + 15f_C z/u_*}, \quad |L| \geq 200\text{m},$$
(2.23)

$$\tau_L = \left(\frac{0.15}{\sigma_u}, \frac{0.07}{\sigma_v}, \frac{0.1}{\sigma_w}\right)\sqrt{h_{\text{ABL}}z}, 0\text{m} < L < 200\text{m},$$
(2.24)

$$[\tau_L]_1 = [\tau_L]_2 = 0.15\frac{h_{\text{ABL}}}{\sigma_u}, -200\text{m} < L < 0\text{m},$$
(2.25)

$$[\tau_L]_3 = \frac{0.1z}{\sigma_w[0.55 - 0.38(z - z_0)/L]}, -200\text{m} < L < 0\text{m and } z$$
$$< 0.1h_{\text{ABL}} \text{ and } z - z_0 < -L,$$
(2.26)

$$[\tau_L]_3 = 0.59z/\sigma_w, -200\text{m} < L < 0\text{m and } z < 0.1h_{\text{ABL}} \text{ and } z - z_0 > -L,$$
(2.27)

provide an analytical solution for a general leaf-area-density profile, respectively. The only forest characteristics that are assumed to be given are tree height (h), canopy depth (Δh_c), stand density (ρ_S), Leaf Area Index (LAI), Diameter at Breast Height (DBH), the extinction coefficient (γ_{ext}), the drag coefficient (C_d) and the roughness length of the forest soil ($z_{0,s}$). In particular, presuming a horizontally homogeneous forest cover, and a number of additional simplifying assumptions, we arrive at an analytical expression for $\overline{u}(z)$, velocity variances, etc. The model consists of an above-canopy model that is matched to an inside-canopy model, which relies on the description of the leaf-area-density. The underlying idea is sketched in Fig. 2. These elements are now successively discussed.

2.2.2.1. Leaf-area density.
The forest canopy model developed below, builds on an available Leaf Area Density (LAD) profile. This study restricts itself to a vegetation canopy with an irregular leaf distribution, mainly present in the upper part of the canopy. Since LAD models in the literature are rather scarce, the model from Porté et al. (2000) for the *Pinus pinaster* is used, for which the LAD [m^{-1}] is given by

$$\text{LAD}(y) = a_1 \cdot y^{a_2} \cdot (a_4 - y)^{a_3} (0 \leq y \leq a_4), y(z) = \frac{z - h_c}{h - h_c}(h_c \leq z \leq h),$$
(2.29)

$$a_1 = \frac{\text{LAI}(a_2 + 1)}{{}_2F_1(a_2 + 1, -a_3; a_2 + 2; a_4^{-1})(h - h_c)}, a_2 = 4.192, a_3 = 1.9264, a_4 \approx 1,$$
(2.30)

with h the tree height [m] and $h_c = h - \Delta h_c$ the height of the bottom of the tree crown [m], LAI the Leaf Area Index [-] and ${}_2F_1$ the hypergeometric function. The values of a_2, a_3 and a_4 correspond with a mature stand that has 2 year-old needles (Porté et al., 2000).

The leaf-area density can be used to characterize the displacement height d of the forest canopy [m], i.e.,

$$d = \frac{\eta\alpha\overline{d}}{\eta(\alpha - 1) + 1}, \quad \overline{d} = \arg_z \max(\text{LAD}(z)),$$
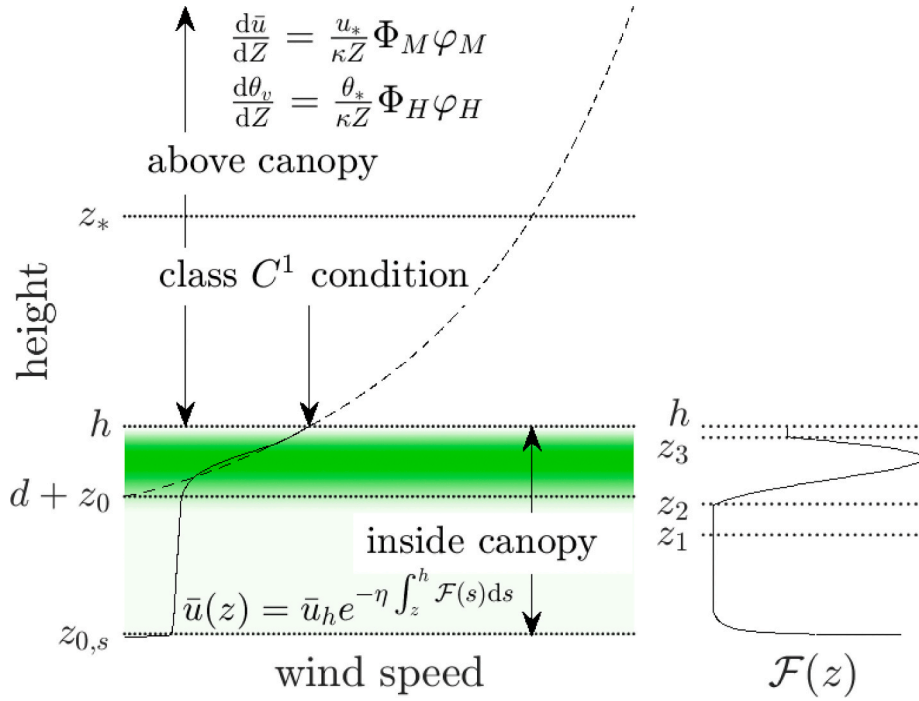(2.31)

Fig. 2. Construction of the canopy parameterization; De Ridder (- -) is matched to a wind measurement $\bar{u}_{\mathrm{ref}}$ above height h and $\bar{u}_h$ at h, continuity is imposed in the gradient and value predictions from De Ridder and Yi (−) at h. The green shading represents the LAD. The right figure displays the graph of the function given by Eq. (2.37). (For interpretation of the references to colour in this figure legend, the reader is referred to the Web version of this article.)

where $\bar{d}$ is the dense-canopy estimate [m], based on Thom (1971), and d is corrected for the sparsity of the forest (Mihailović et al., 1999). A formula for α and η is given by (A.19); a justification can be found at the end of the next section ('Above-canopy model').

2.2.2.2. Above-canopy model. The above-canopy wind profile can be modeled by means of a similarity scaling argument. It is a known fact that a forest can influence the flow up to five times its own height (Raupach et al., 1991). The perturbed layer is referred to as the roughness sublayer and its effect needs to be incorporated. To that end, the similarity scaling formulation from Physick–Garratt with the roughness-sublayer correction from De Ridder (2010) is used. Alternative models can be found in Mihailović et al. (1999), but the drawback is that their gradient does not converge to the one of the classical log law for $z \gg h$.

Take u_* the friction velocity at the canopy top, and z_* thickness of the roughness sublayer [m], then the wind speed above the canopy is described by (De Ridder, 2010)

$$\frac{\mathrm{d}\bar{u}}{\mathrm{d}Z}(Z; u_*, \mu_M, L) = \frac{u_*}{\kappa Z} \Phi_M(Z/L) \varphi_M(Z/Z_*; \mu_M), \quad Z := z - d, \quad z > z_0 + d,$$
(2.32)

with d the displacement height (see Eq. 2.31), Φ_M the stability kernel

function from Dyer (1974) (as in section §2.2.1), $\varphi_M(x; \mu_M) = 1 - \exp\{-\mu_M x\}$ the roughness-sublayer kernel function for momentum, $z_0 = 0.071h$ the roughness length (Mölder and Lindroth, 1999) and $Z_* = 2h - d$ for a pine forest (Mölder et al., 1999).

Integrating Eq. (2.32) from z_0 to Z leads to the following expression for the wind speed

$$\Psi_M^*\left(\frac{Z}{L}, \frac{Z_*}{L}; \mu_M\right) = \int_Z^\infty \frac{\Phi_M(z'/L)}{z'} e^{-\mu_M z'/z_*} \mathrm{d}z'$$
$$\approx \Phi_M\left[\left(1 + \frac{1}{2\mu_M} \frac{Z_*}{Z}\right) \frac{Z}{L}\right] \frac{2}{3} \ln\left(1 + \frac{3}{2} \frac{Z_*}{\mu_M Z}\right) \exp(-\mu_M Z/Z_*),$$
(2.34)

where Ψ_M is the integrated form of the kernel function Φ_M, see (A.10-A.11).

A similar reasoning can be applied to the temperature profiles; the friction velocity is replaced by the temperature scale θ_*, the roughness length z_0 by $z_{0,H}$ such that $z_{0,H} + d$ is the height at which the ground temperature is measured and the kernel function for heat should be used in stead of the one for momentum, hereafter denoted by the subscript H instead of M. The unknown parameters are the friction velocity u_*, the temperature scale θ_*, the Monin-Obukhov length L and the empirical parameters μ_M and μ_H introduced by De Ridder (2010).

The model of De Ridder requires two emperical parameters μ_M and

$$\bar{u}(Z; u_*, \mu_M, L) = \frac{u_*}{\kappa}\left(\ln\left(\frac{Z}{z_0}\right) - \Psi_M(Z/L)\right.$$
$$\left. + \Psi_M(z_0/L) + \Psi_M^*\left(\frac{Z}{L}, \frac{Z}{Z_*}; \mu_M\right) - \Psi_M^*\left(\frac{z_0}{L}, \frac{z_0}{Z_*}; \mu_M\right)\right),$$
(2.33)

μ_H. Average values can be found in De Ridder (2010) for the considered type of forest. However, the opinion of the authors of the current work is that these values don't work well for every type of forest. Therefore, we propose to estimate these parameters as well from the meteo data. Consequently, another wind speed and virtual potential temperature measurement is required, preferably in the roughness sublayer. Assume that the wind speed is also known at the canopy top ($\overline{u}_h$), that the variation in potential virtual temperature is known above ($\Delta\theta_{v,\text{ref}}$) and in ($\Delta\theta_{v,0}$) the canopy w.r.t. the temperature into the canopy ($\theta_{v,0}$). In order to predict the temperature above the canopy, the ground temperature should be measured between height d and h. Further on, the atmosphere inside the canopy is postulated to be neutral. Since the potential virtual temperature is height independent in a neutral atmosphere (e.g., see Holton, 2004), $z_{0,H} = z_0$ can be assumed in case the ground temperature is measured at a lower height than d. Given the above-canopy measurements $\overline{u}_{\text{ref}}$ and $\Delta\theta_{v,\text{ref}}$, together with $\overline{u}_h$ and $\Delta\theta_{v,0}$, the unknown parameters are calculated by solving a system of the form

$$\begin{cases} \overline{u}\left(z_{\text{ref}} - d; u_*, \mu_M, L\right) & = & \overline{u}_{\text{ref}} \\ \overline{u}(h - d; u_*, \mu_M, L) & = & \overline{u}_h \\ L & = & \dfrac{u_*^2 \theta_{v,0}}{\kappa g \theta_*} \\ \theta_v\left(\overline{z}_{\text{ref}} - d; \theta_*, \mu_H, L\right) - \theta_{v,0} & = & \Delta\theta_{v,\text{ref}} \\ \theta_v(h - d; \theta_*, \mu_H, L) - \theta_{v,0} & = & \Delta\theta_{v,0} \end{cases} \quad (2.35)$$

This strategy to determine the unknown parameters can be regarded as a variation on the profile method.

Unfortunately, our experiments did not provide measurements for $\overline{u}_h$ and $\Delta\theta_{v,0}$ (or other measurements inside the canopy). Therefore, we estimate $\overline{u}_h$ and $\Delta\theta_{v,0}$ from the model of Mihailović et al. (1999). This model describes the wind speed and temperature profile in the lower part of the roughness sublayer, hereby taking the sparsity of the canopy into account by means of a surface correction Γ_1. According to Mihailović et al. these profiles, denoted u_M and $\theta_{v,M}$, are described by

$$\frac{d\overline{u}_M}{dZ} = \frac{u_*}{\kappa \Gamma_1 Z}\Phi_M, \quad \frac{d\theta_{v,M}}{dZ} = \frac{\theta_*}{\kappa \Gamma_1 Z}\Phi_H, \quad Z \overset{+}{\to} h - d.$$

Here, $\Gamma_1 = \eta(\alpha - 1) + 1$ with $\alpha^2 = 4(C_d \cdot \text{LAI})^{1/2}$ in case of a forest, C_d the effective drag coefficient [-] and η the plant cover [-]. Using the same analogy as in Brisson et al. (1992), the plant cover can be characterized as $\eta = 1 - \exp(-\gamma_{\text{ext}}\text{LAI})$ with γ_{ext} the extinction coefficient [-]. The value of γ_{ext} for a Scots pine (the variety at the SCK CEN site) is 0.526 (Lindroth and Perttu, 1981). Let $\overline{u}_h \approx u_M(h; u_*, L)$ and $\Delta\theta_{v,0} \approx \theta_{v,M}(h; \theta_*, L) - \theta_{v,0}$, then system (2.35) can be solved. Notice that the model of Mihailović et al. can adapt to the meteorological situation, because it is related to the available measurements through the parameters u_*, θ_* and L in system (2.35).

2.2.2.3. Inside-canopy model. For the inside-canopy model, we slightly adapt the approach from Yi (2008). In the original approach, the flow inside the canopy is described by the two-dimensional momentum equation as follows

$$\frac{d\tau}{dz} = \rho C_d \text{LAD} u^2. \quad (2.36)$$

This equation contains two unknowns: the shear stress τ and the wind speed u. Therefore, a closure assumption is needed. Vegetation canopies that have a strongly varying leaf distribution over height, are preferably described by a variable LAD. To the authors' knowledge, the only closure assumption in the literature that allows solving (2.36) analytically with a variable LAD profile, corresponds to $\tau = \rho C_d u^2$. A more detailed description about the resulting model can be found in Yi

(2008).

The main drawback of this model is that a zero velocity gradient is imposed at the canopy top, such that a smooth coupling with an above-canopy wind model is not possible. Therefore, we propose to overcome this issue by replacing the LAD by the function $\mathcal{F}(z)$ [m^{-1}] i.e.

$$\mathcal{F}(z) = \begin{cases} \dfrac{1}{\eta L_s} & , z_3 \leq z \leq h \\ \text{LAD}(z) & , z_2 \leq z < z_3 \\ \dfrac{\pi}{2}\rho_S \text{DBH} & , z_1 \leq z < z_2 \\ \dfrac{z_1}{z} \cdot \mathcal{F}(z_1) & , 0 \leq z < z_1 \end{cases} \quad (2.37)$$

with ρ_S the stand density [trees/m^2], DBH the diameter of the trunk at breast height [m], and $L_s = \overline{u}_h/\overline{u}_h'$ [m] the Raupach shear length scale (Raupach et al., 1996) where $\overline{u}_h$ and $\overline{u}_h'$ are shorthand notations for (2.33) and (2.32) evaluated in $z = h$ respectively. Below height z_1 the wind profile is assumed to be perturbed by the ground-surface roughness elements. Denote the aerodynamic roughness length of the forest soil by $z_{0,s}$, then Blocken et al. (2007) suggests that the height of the roughness layer is much larger than $z_{0,s}$, which motivates the choice $z_1 = 10z_{0,s}$. In this layer, zero wind speed is imposed at the bottom and the $1/z$ form is chosen such that this condition is enforced (see (2.38)). The heights z_2 and z_3 are determined by imposing continuity conditions i.e. by solving

$$\text{LAD}(z_3) = \frac{1}{\eta L_s}, \quad \text{LAD}(z_2) = \frac{\pi}{2}\rho_S \text{DBH}.$$

The first line in (2.37) arises from gradient-fixing with the roughness-sublayer model (2.32). The third line represents the frontal area of the trunks per unit volume of canopy. The last line represents the influence from the soil and this form is chosen such that $\overline{u}(z) \to 0$m/s as $z \to 0$m in (2.38).

Before being able to solve (2.36), we require a further parametrization of C_d. In vegetation canopies, the drag coefficient dependents on the local wind speed, and typically $C_d \propto u^{-r}$ with $r > 0$ (Vogel, 1984). For the upper part of the canopy of a pine tree, one can roughly estimate $r \approx 1$, see Vogel (1984), Table 1, p.40. Assuming this relationship, (2.36) can be reformulated into $d\overline{u}/dz = F(z)\overline{u}/(2 - r)$, which has the following analytical solution,

$$\overline{u}(z) = \overline{u}_h e^{-\frac{\eta}{2-r}\widehat{L(z)}}, L(z) = \int_z^h \mathcal{F}(s)ds, z \leq h, \quad (2.38)$$

with η chosen the same as in the above-canopy model.

Equations (2.4) and (2.6) also require $\tau_L(z)$ and $\sigma_u(z)$ for the dispersion simulation. To estimate $\tau_L(z)$ above the canopy, (2.23-2.28) are evaluated at $z = h_{\text{eff}} - d$. If the stack height is lower than the canopy height, τ_L is evaluated at $z = h - d$. Above the canopy, σ_u is as discussed in §2.2.1. Inside the canopy, σ_w decreases linearly to one tenth of its value at height z_*. A justification of this assumption can be found in
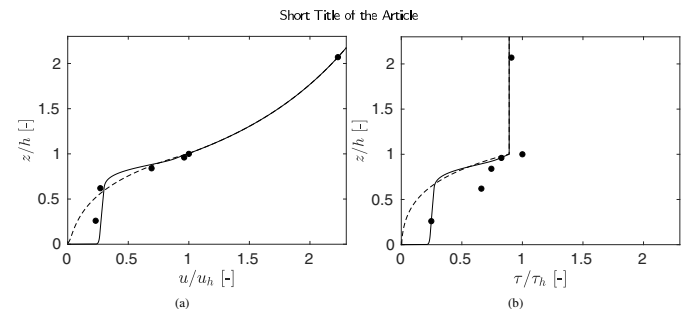

Fig. 3. Predictions by the F (—) and Wang's model (Wang, 2012) (- -), measurements (●) (Sellier et al., 2008). (a) Wind speed, (b) Reynolds stress.

Wilson and Shaw (1977, Fig. 3, p.1203). The variation of σ_w over height in the roughness sublayer is rather complex. So in case of an unstable atmosphere, σ_w is kept constant with $\sigma_w(z) = \sigma_w(z_* - d)$ for $h \leq z \leq z_*$. The parameter set-up inside the canopy is similar to Legg and Raupach (1982).

2.3. Computational set-up

During BR1 operation, Ar-41 gas is assumed to be released at a typical temperature of 298.15 K, with a release exhaust velocity of 1.5 m/s. Ar-41 is a noble gas with a half-life of 1.8 h and $E_\gamma = 1.294$ MeV, so that the radioactive decay rate can be neglected over the advection time through our computational region of interest (approximately 1 min for a stack release and average wind speed). Unfortunately, the exact value of the source Q is uncertain. Different values are given in different references, for this reason two values spanning the range have been adopted: $Q_1 = 57$ GBq/h (Pauly et al., 1997), and $Q_2 = 150$ GBq/h (Rojas-Palma et al., 2004). Both will be used in the current study. See further section 4 for a discussion.

Systems (2.20) and (2.35) are solved using fixed-point iteration (e.g., Adams and Essex, 2010, §4.2 p.220). Note that the equations in (2.35) only have a non-linear dependence on the variables μ_M and μ_H. Therefore, μ_M and μ_H are solved from the second and fifth equation respectively using Newton's method. If during the iteration the value of μ becomes negative, Newton's method is stopped immediately and the fixed-point iteration is continued with the last positive value. The fixed-point iteration is initialized with $L \to \infty$ for both (2.20) and (2.35). The value used for μ_M to initialize Newton's method in the first fixed-point iteration is the average value 2.59 reported in De Ridder (2010). Since μ_H satisfies the same equation in the neutral case, the value of μ_M is adopted. A first estimate of u_* and θ_* is obtained by continuing with the fixed-point iteration. The fixed-point iteration is stopped if the residual drops below 10^{-4}. Since the meteorological data is only known up to two digits, this threshold is considered to be sufficient.

In order to solve (2.3,2.4) and (2.3,2.6), the initial condition $\mathbf{X}_0 = (0, 0, h_{\text{eff}})$ is used, and $(0, 0, 0)$ for $\mathbf{u}'_p$. The effective stack height h_{eff} is calculated using the maximum plume rise by Brigg's formulas (Briggs, 1982). Next to a stack release, we will also consider simulations with a ground release. In this scenario, we expect that the plume will be trapped within the forest canopy. Therefore, we do not apply Brigg's correction for plume rise if we are modeling a forest canopy combined with a ground release.

All the Lagrangian models have been implemented in C++. Particle trajectories are calculated completely meshfree. The size of the domain is $4000 \times 4000 \times 500$ m³. At the bottom of the domain, a reflective boundary is imposed. For every meteo record, an optimized time step has been selected such that the condition $0.01[\tau_L]_k \leq \Delta t \leq 0.5[\tau_L]_k$ (Legg and Raupach, 1982) is satisfied for $k = 1, 2, 3$. Equivalently, Δt should satisfy $0.01 \max_k [\tau_L]_k \leq \Delta t \leq 0.5 \min_k [\tau_L]_k$. The time step remains fixed as long as the meteorological conditions are not updated.

The data to be simulated is divided into blocks. Each block consists of 25 10-min records and all blocks belong to a different day of the year. Before the simulation of one block starts, a spin-up period of 10 min is inserted such that the initial condition of a mature plume is reached. Subsequently, dose-rate statistics were accumulated during 10 min. For both the stack and ground release, $N_p = 5 \cdot 10^4$ particles per time step were released. We verified that the combination of time step, time horizon and number of particles led to a sufficiently converged dose rate. To this end, five days from the NERIS data set, described in §3, were selected such that they are representative for all the different meteorological conditions occurring during the experiment. Each of these days was simulated with $2N_p$ particles released per time step. The dose rates from the LT–F model were found to be the least converged with an average deviation of 1.15% for the stack release and 0.91% for the ground release.

The Gaussian plume model has been implemented in the mathematical software package MATLAB. For this, a Cartesian structured mesh consisting of 7.2 million hexahedral cells was used. The size of the computational domain is $2000 \times 600 \times 200$ m³. In order to evaluate the dose rates, the integral (2.1) is discretized. This discretization requires a mesh. As opposed to the Lagrangian models, the concentration value, provided by the Gaussian model, can now be directly substituted. The vertical mesh is finest over the lowest 80 m with a cell height of 1 m. The vertical resolution was coarsened near the top. The cells at the top of the domain have a vertical size of 10 m. The expansion ratio varies slightly over the vertical direction, but remains always around two for the part higher than 80 m (one otherwise). The horizontal mesh resolution is 5 m. Changing wind directions are taken into account by rotating the monitoring stations and keeping the plume direction fixed.

3. Results

The routine Ar-41 releases originating from the air-cooled-graphite-moderated BR1 reactor at the Belgian Nuclear Research Centre (SCK CEN) are the subject of this study. The site is depicted in Fig. 1. One can observe that the site is partly covered by forest, which is a monocultural Scots pine stand of approximately 60 years old. During a field campaign in 2005, the height and diameter at breast height of 161 trees at the SCK CEN site were measured. This resulted in a mean height (h) of 22.4 ± 3.7m and a mean DBH of 0.29 ± 0.05m. The stand density ($\rho_S = 359$ trees/ha) and annual variation of LAI (average value of 2.2) were measured as well. Details about the campaign can be found in (Vincke, 2006; Vincke and Thiry, 2008). The Ar-41 is released to the environment through a 60 m-high chimney, which is surrounded by seven stations of the Belgian early warning network TELERAD (Sonck et al., 2010). The red marks in Fig. 1 show the location of the TELERAD stations. The fact that all these stations are located in forest area motivates the use of a canopy model. Note that one station, IMR/M11, is located outside the actual forest near a building (see Fig. 1). Therefore, the used forest-roughness approximation might be too crude for simulating the effect of ground releases at this station properly. The authors believe, however, that the effect of stack releases at IMR/M11 is well simulated using this approximation since it seems unlikely that a strong interaction between the plume and the respective building occurs over the short distance to the chimney. The monitoring stations provide the ambient gamma dose rates (i.e. strictly speaking the ambient dose equivalent rate, usually denoted as $\dot{H}^*[10]$). The data spans 16 days in the first half of 2017, with 25 consecutive 10-min periods per day. In-situ weather data were provided by the met mast, located at a distance of 425 m from the stack. The mast provides the mean wind speed, azimuth, elevation, and their standard deviations at 69 m, and the temperatures at 114 m and 8 m. All these measurements are 10-min averaged quantities. Since relative-humidity measurements are not conducted, a standard value of 80% is assumed (annual average of Brussels). Based on the in-house classification (Bultynck and Malet, 1972), 12 days were prevailingly (slightly) unstable, 3 days were prevailingly neutral and 1 day was slightly stable. This experimental dataset was also distributed in context of the NERIS atmospheric dispersion modeling experiment (Camps, 2018). Here, members of the European Platform on preparedness for nuclear and radiological emergency response and recovery (NERIS) were invited to participate.

3.1. Canopy wind profile and stability estimation

Unfortunately, meteorological data inside the SCK CEN forest are not available. Therefore, we validate the forest canopy model versus data from Sellier et al. (2008) in which the Bray forest (France) was investigated. This forest is an ideal test case for the canopy model because the LAD model (Porté et al., 2000) was developed for this forest site and it exhibits similar characteristics as the SCK CEN forest: even-aged trees

Table 4
Parameter values used for validation of the canopy model.

h	LAI	γ_{ext}	ρ_S	DBH	h_c	C_d	z_{ref}	$\overline{u}_{ref}$	z_0	$z_{0,s}$	a_0
20.7 m	1.83	0.526	386 trees/ha	0.316 m	10.7 m	0.26	42.85 m	5.8 m/s	1.0 m	0.25 m	0.088 m^{-1}

and a comparable canopy structure, stand density, canopy height and diameter at breast height (DBH). Temperature measurements are not given, so we assume neutral stratification. Taking the limit from (2.35) for $L \to \infty$ yields

$$\begin{cases} \overline{u}(h-d; u_*, \mu_M) & = \dfrac{u_*}{\kappa \Gamma_1} \ln\left(\Gamma_1 \dfrac{h-d}{\alpha^2 z_0}\right) \\ \overline{u}(z_{ref} - d; u_*, \mu_M) & = \overline{u}_{ref} \end{cases} \qquad (3.1)$$

which needs to be solved for u_* and μ_M. The values $\alpha = 1.7$ and $\Gamma_1 = 1.4$ are obtained from (A.19) using the values provided in Table 4. Then, $d = 12.8$ m follows from (2.31).

Fig. 3a shows the measurements together with the predicted wind profile (solid line). It is clear that the behavior of the measurements is well captured and that the wind speeds are closely approximated. For the sake of completeness, also the prediction of the Reynolds shear stress is shown in Fig. 3b; the model formulation can be found in Yi (2008) in which the LAD is replaced by $\mathscr{F}$. Although the stresses at and above the canopy top are well captured, the behavior inside the canopy is less well represented. This is to be expected since the model only uses a first-order turbulence closure. Using a higher order closure can improve the stress predictions (Raupach and Thom, 1981) inside the canopy, but this is beyond the scope of the current research. We further observe that the stress at the canopy top is well represented. Thus, the validation shows that the proposed model is capable of producing a realistic canopy wind

profile and estimating the friction velocity at the canopy top.

In order to stress the importance of using a variable-LAD model, also the wind profile obtained from Wang's constant-LAD model (Wang, 2012) is shown. The parameter a_0 in Table 4 represents the constant leaf area density, which was evaluated as LAI/h. Wang's model approximates the wind speed in the crown of the trees well, but the behavior below the crown is not captured. This is also a reported deficit of the widely used constant-LAD model of Inoue (Raupach and Thom, 1981). This motivates the choice for the variable-LAD model from Yi (2008).

We further evaluate the stability estimation obtained through the proposed canopy model. A reliable way to verify the stability classification based on the value of the Monin-Obukhov parameter L is the Eddy Covariance Method. The application of this method yields an accurate calculation of u_* and θ_* by using high-frequency measurements such that L can be accurately estimated. Unfortunately, high-frequency measurements are not available and therefore, the stability classification is compared with the in-house method, by Bultynck and Malet. Instead of L, $[\partial\theta/\partial z]/u(69m)^2$ is used here as a stability parameter. See Ref. (7) for more details. The stability parameter L is solved from (2.20) or (2.35) depending whether the OF or F model is used respectively. The stability classification system based on L has been taken from Gryning et al. (2007). All the meteorological data from the NERIS experiment, 400 records, are used for this comparison. The results are presented in Fig. 4.

It can be immediately observed that the model choice has a clear influence on the stability classification. The F model, Fig. 4c, compares
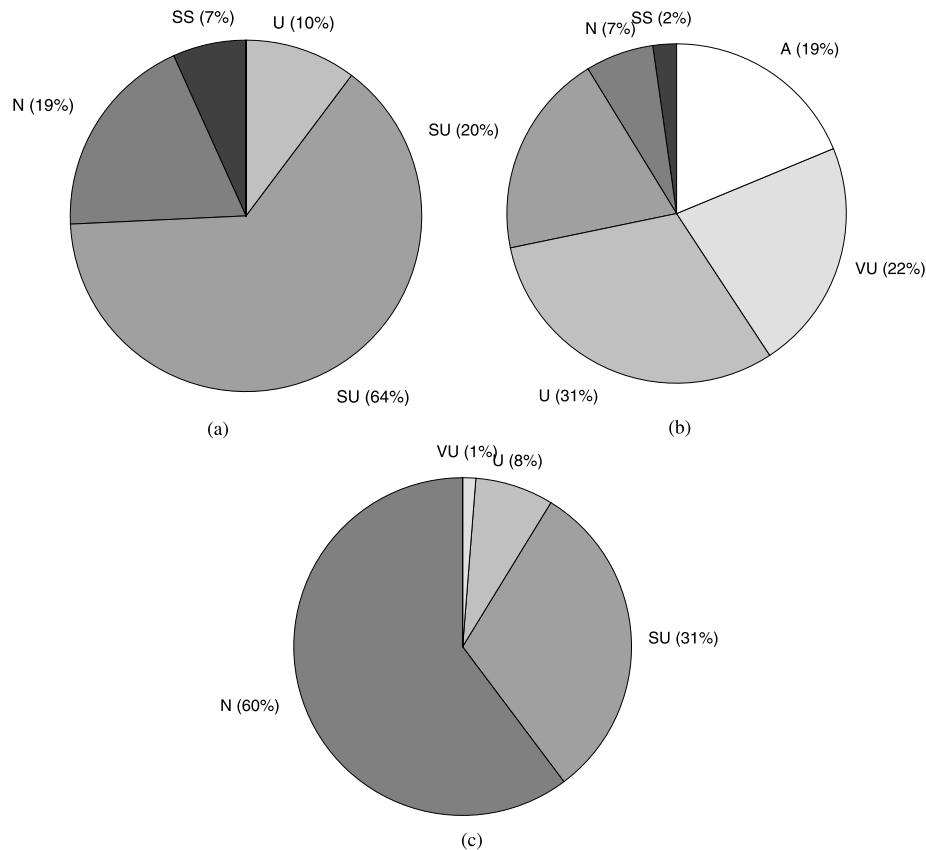

Fig. 4. Stability classification according to the (a) in-house method, (b) OF model and (c) F model. Abbreviations stand for slightly stable (SS), neutral (N), slightly unstable (SU), unstable (U), very unstable (VU) and anomalous (A).

Table 5

Model comparison for source strength $Q_1 = 57$ GBq/h. The abbreviation M stands for measurement and the model names G–PG, G–BM, LB–OF, LB–F, LT–OF and LT–F are the same as in Table 2.

release height [m]	$\dot{d}_{\gamma,o}$	$\dot{d}_{\gamma,p}$	FB [-]	NMSE [-]	FAC2 [-]	MRM [-]	Not rejected [#]
60	M	LB–F	1.21	4.0	0.04	0.25	1028
	M	LB–OF	1.18	3.67	0.05	0.27	1028
	M	LT–OF	1.10	3.02	0.08	0.31	1028
	M	LT–F	0.85	1.68	0.27	0.44	1028
	M	G–BM	1.05	2.67	0.09	0.33	1028
	M	G–PG	1.10	3.02	0.08	0.31	1028
	G–PG	LB–F	0.18	0.07	1.0	0.81	878
	G–PG	LB–OF	0.12	0.03	1.0	0.87	878
	G–PG	LT–OF	0.01	0.03	1.00	1.0	878
	G–PG	LT–F	− 0.32	0.20	0.98	1.43	878
	G–PG	G–BM	− 0.07	0.01	1.00	1.06	878
10	G–PG	LB–F	− 1.46	20.95	0.03	6.2	1880
	G–PG	OF	0.33	3.05	0.82	0.74	1880
	G–PG	LT–OF	0.28	0.47	0.98	0.80	1880
	G–PG	LT–F	− 0.61	1.09	0.46	1.67	1880
	G–PG	G–BM	− 0.30	0.33	0.99	1.38	1880

more favorably with the in-house method, Fig. 4a, than the OF model, Fig. 4b. The F model predicts 9% of the data to be non-neutral, while for the in-house method this amounts to 10%. The OF model predicts 72% to be non-neutral. The anomalous values correspond to values of L that are close to zero, $-50\text{m} < L < 10\text{m}$, such that they fall outside the range used in the classification from Gryning et al. (2007). It should also be observed that anomalous values of L are not occurring by using the F model. Note that the roughness-sublayer correction reduces the temperature difference between the temperature at measurement and tree height. This explains why unstable conditions are less occurring with the F model. Whether the distinction between neutral and near-neutral (slightly (un)stable) is well predicted is of lesser importance since the dispersion parameterization is only altered for non-neutral conditions.

3.2. Model comparison

The simulated dose rates from the different models were compared for stack and ground releases. In case of stack releases, the simulated dose rates are compared with the measured ones. For the ground releases, no experiments are available. The same meteorological data is assumed as for the stack releases, but instead the release height is set to 10 m. We added this case for further comparison of the models.

A comparison is elaborated using the performance measures introduced by Chang and Hanna (2004). These measures include the fractional bias (FB), the geometric mean bias (MG), the normalized mean square error (NMSE), the geometric variance (VG) and the fraction of predictions within a factor of 2 of observations (FAC2). Since the measurements vary with maximum one order of magnitude, MG and VG are not relevant (see Chang and Hanna, 2004 for an explanation). The expressions of the FB, NMSE and FAC2 are as follows

$$FB = \frac{\left(\overline{\dot{d}_{\gamma,o}} - \overline{\dot{d}_{\gamma,p}}\right)}{0.5\left(\overline{\dot{d}_{\gamma,o}} + \overline{\dot{d}_{\gamma,p}}\right)},$$

$$NMSE = \frac{\overline{\left(\dot{d}_{\gamma,o} - \dot{d}_{\gamma,p}\right)^2}}{\overline{\dot{d}_{\gamma,o}} \, \overline{\dot{d}_{\gamma,p}}},$$

$$FAC2 = \text{fraction of data that satisfy } \frac{1}{2} \le \frac{\dot{d}_{\gamma,o}}{\dot{d}_{\gamma,p}} \le 2,$$

where the bar denotes the average over the dataset, $\dot{d}_{\gamma,p}$ are the model predictions and $\dot{d}_{\gamma,o}$ the observations. The observation can be virtual (prediction from an other model) or a field measurement. In addition, we will also consider the mean ratio of the maximum values (MRM) i.e. $\overline{\dot{d}_{\gamma,p,max}/\dot{d}_{\gamma,o,max}}$.

For the stack releases (60 m), dose rate measurements are available and therefore the performance of the models can be assessed according to the above measures. For the ground releases (10 m), no measurements are available. The best that can be achieved for the latter is assessing the difference between the models. In order to do this, the above measures are evaluated using the predictions of the G–PG model as a reference since this is a widely known model. It should be emphasized that a deviating model performance w.r.t. the G–PG model is not necessarily problematic, but only points to large differences to a common and standard model. Results are displayed in Table 5 and 6, including the number of data points that are used in the calculation. A data point is rejected when the observation is not available or when it has a value below 10 nSv/h. This threshold has been chosen to remove noise. The average background radiation is around 78 nSv/h. The SARA detectors have a maximum bias of 10%, and a random error with a maximum of 6

Table 6

Model comparison for $Q_2 = 150$ GBq/h. The abbreviations are the same as in Table 2.

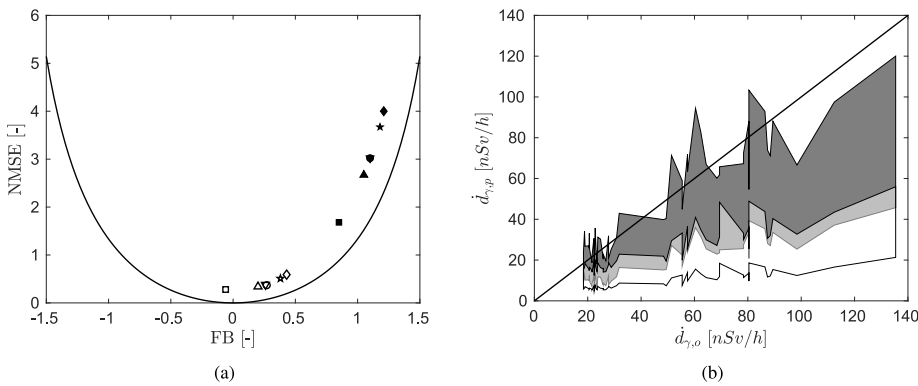| release height [m]	$\dot{d}_{\gamma,o}$	$\dot{d}_{\gamma,p}$	FB [-]	NMSE [-]	FAC2 [-]	MRM [-]	Not rejected [#]
60	M	LB–F	0.43	0.59	0.73	0.66	1028
	M	LB–OF	0.38	0.51	0.75	0.71	1028
	M	LT–OF	0.27	0.37	0.79	0.81	1028
	M	LT–F	− 0.06	0.28	0.83	1.15	1028
	M	G–BM	0.20	0.34	0.83	0.87	1028
	M	G–PG	0.26	0.38	0.81	0.82	1028

Fig. 5. (a) FB and NMSE for all models when compared with the measurements in case of Q_1 (filled symbols) and Q_2 (open symbols); LT-F (□), LT-OF (○), LB-F (◇), LB-OF (★), G-F (△), G-OF (▽); the curve shows the systematic error component of the NMSE versus FB, (b) plot of the predicted dose rates ($\dot{d}_{\gamma,p}$) by the LT–F (dark shading) and LB–F (white shading) model w.r.t. the measured ones ($\dot{d}_{\gamma,o}$) in stations IMR/M08 and IMR/M13 on 2017/05/04; the shading indicates the region of uncertainty due to the uncertain source strength.

nSv/h, motivating the choice of the 10 nSv/h noise threshold. It should also be mentioned that the measured dose rates have been corrected for background radiation.

We compare the models in the measurement points; in this and the next paragraph we focus on the stack releases. To this end, consider the statistics in Table 5, using source strength Q_1, resulting from the comparison with the measurements (M). We observe that the performance statistics for all the models, apart from the LT–F model, are similar. The best performing model is the LT–F model and the worst is the LB–F model. From the FB statistics can be inferred that the arithmetic average of the data set is underestimated by a factor of 3–4. The LT–F model performs slightly better, underestimating by a factor of 2.5. Also note that there is a one-to-one relationship between the MRM and FB. As an example, the LB–F model underestimates the arithmetic average of the dataset by a factor of 4.1 (see FB value) while the maximum value is underestimated by a factor of 4 on average (see MRM value). Similar conclusions can be drawn for the other models. The fact that FB is a measure of systematic model error implies that the prediction error on the observed dose rate closest to the plume centerline (the highest values) is the main source of systematic error. The NMSE is a measure of both systematic and random error; the curve in Fig. 5a indicates the systematic error component. Moreover, from the FB can be inferred that for each model, the NMSE is determined approximately for 56% by systematic errors for each model. The presence of systematic errors

means that the predictive skill for each model can be further improved. The LT–F model has the lowest absolute random error and consequently it is the model with the most predictive skill. This is also clearly illustrated in Fig. 5a (filled symbols).

Since the source strength is uncertain (as mentioned in §2.3), Table 6 displays the statistics from Chang and Hanna for source strength Q_2. Similar conclusions can be drawn as in the previous paragraph. The LT–F model is still the best performing model and it is the only model with a negligible bias. The bias of the other models has improved to a factor of 1.2–1.5 underestimation on average. Also remarkable is that the contribution of the systematic error to the NMSE differs more strongly between the models; see Fig. 5a (open symbols). The contribution is the highest for the LB–F and LB–OF model i.e. 30%. The NMSE of the LT–F model is almost completely determined by random errors, only 1.2% is due to systematic errors. For the other models, the contribution lays between 10% and 20%. Now, the models can be less well discriminated based on the FAC2 measure, which is approximately 80% for all the models. A typical simulation result for the best (LT–F) and worst (LB–F) performing model is shown in Fig. 5b. The LT–F model approximates the dose rates better than the LB–F model for both source strengths. For Q_2, the LT–F model also approximates the bisector of the plane well with a tendency to underestimation for dose rates higher than 90 nSv/h. In general, the statistics have clearly improved with Q_2.

We now compare the models for the ground (10 m) release. It can be

Table 7

(a) Meteorological cases and (b) parameter values for the sensitivity analysis, (c) SI values for each parameter at three detector distances (120 m, 185 m and 235 m).

(a)

case	L [m]	$\bar{u}$ [m/s]	σ_{azi} [°]	σ_{elev} [°]
1	− 615	5.6	12.8	8.4
2	− 80	2.7	19.5	16.3
3	− 291	4.1	20.6	10.9
4	− 226	2.8	59.3	17.5

(b)

	h [m]	LAI [−]	DBH [m]	Δh_c [m]	C_d [−]	L [m]	$\bar{u}$ [m/s]	wind direction [°]
default	22.4	2.2	0.29	10.0	0.2	/	4.1	0
min	15	1.0	0.1	5.0	0.05	− 80	2.4	0
max	35	3.43	0.5	15.0	0.8	∞	5.8	119
case	1	1	1	1	1	2	3	4
reference	Vincke (2006); Gielen et al. (2016)	Vincke and Thiry (2008); Vincke (2006)	Vincke (2006); Gielen et al. (2016)	/	Yi (2008)	(see text)		

(c)

distance	h	LAI	DBH	Δh_c	C_d	L	$\bar{u}$	wind direction
120 m	0.33	0.27	0.01	0.05	0.19	0.23	0.38	0.56
185 m	0.30	0.28	0.01	0.04	0.18	0.22	0.40	0.65
235 m	0.20	0.24	0.01	0.01	0.10	0.22	0.41	0.72

seen from Table 5 that the LB–F, LT–F and G–BM model predict higher dose rates than the G–PG model, while the LT–OF and LB–OF model predict lower ones; see the FB. Nonetheless, the LT–OF and G–BM model have a very similar performance as the G–PG model w.r.t. the NMSE and FAC2 measure. So, it seems that not much accuracy is gained by using a high-roughness parameterization for a Gaussian model, not even for a ground release. The LB–F model deviates the most from the G–PG model. As can be inferred from the FB measure, the LB–F model estimates the dose rates on average roughly a factor of 6 higher than the G–PG model. It is also clear from the FAC2 measure that the discrepancy between both models is more apparent for the ground than for the stack releases. For the stack releases, 90% of all the model predictions falls within a factor of 2.2 of each other, whereas for the ground releases 90% falls within a factor of 14.

3.2.1. Sensitivity analysis

Since the forest canopy model contains a substantial amount of parameters that are usually only roughly known, we perform a sensitivity analysis. An upper bound of the sensitivity for each variable can be estimated using the sensitivity index (SI). The sensitivity of a quantity D w.r.t. a parameter p is then given by (Hamby, 1994)

$$SI(D) = \frac{D_{\max} - D_{\min}}{D_{\max}}, \quad D_{\max} := \max\{D(p_{\min}), D(p_{\max})\}, \quad D_{\min}$$
$$:= \min\{D(p_{\min}), D(p_{\max})\}$$

in which the common values of p are assumed to be confined to the interval $[p_{\min}, p_{\max}]$. The investigated parameters are tree height h, LAI, diameter of the trunk at breast height DBH, the canopy depth Δh_c, the effective drag coefficient C_d, the effect of stratification (L), wind speed $\overline{u}$ and wind direction. The default, minimum and maximum values of each parameter are displayed in Table 7b. These values are based on available measurements or on values cited in the literature (see references in Table 7b).

Four cases are selected for the meteorological parameters (see Table 7a). Case 1 represents the conditions at the observed median value of L (2017/05/04 at 13:40); Case 2 corresponds to the conditions at $\min|L|$ (2017/05/03 at 15:50); Case 3 corresponds to conditions of maximal wind speed variation over half an hour i.e. $\overline{u}$ is limited to $[\min\{\overline{u}_{I-1}, \overline{u}_I, \overline{u}_{I+1}\}, \max\{\overline{u}_{I-1}, \overline{u}_I, \overline{u}_{I+1}\}]$ such that $\left|\overline{u}_{I+1} - \overline{u}_I\right|$, $\left|\overline{u}_I - \overline{u}_{I-1}\right|$ or $\left|\overline{u}_{I+1} - \overline{u}_{I-1}\right|$ is maximal with $\overline{u}_I$ the I-th wind speed record (2017/04/18 at 14:10); Case 4 corresponds to the conditions at $\max\sigma_{azi}$ (2017/04/18 at 11:50).

In Table 7c, we investigate the sensitivity of dose rates measured at three detectors for those selected conditions. These are located at ground level at 120 m, 185 m and 235 m downstream from the BR1 chimney. These distances correspond to the minimal, average and maximal distance respectively from a detector to the BR1 chimney. The sensitivity is conducted for the LT–F model since this model reproduced the measurements the best. The dose rates are most sensitive to the wind direction and the wind speed $\overline{u}$. The most sensitive forest characteristics are the LAI and tree height h, whereas predictions are insensitive to DBH and Δh_c. The dose rate calculation is moderately sensitive to C_d. Clearly, the model bias cannot be attributed to the sensitivity of the individual forest characteristics. Only the sensitivity to the wind direction is plausible.

4. Discussion

The Langevin models distinguish themselves from the other models by their capability of taking the autocorrelation of the particle's velocity into account. Since no decisive value has been obtained for the source strength, the most objective observation is that there are performance differences between the models. In particular, the LT–F model tends to

perform better than the other models. Note that the LB–F model has the same terrain parameterization as the LT–F model, but does not take the autocorrelation into account. The LT–OF model, on the contrary, does take the autocorrelation into account, but it has a different terrain parameterization. Both models perform differently than the LT–F model, which suggests that both the autocorrelation and the terrain roughness modeling are important aspects.

It is somewhat surprising that the performance of the two Gaussian models is closer to the models based on the Langevin equation (LT–OF and LT–F) than to the ones derived from the general advection-diffusion equation (LB–OF and LB–F). As explained in section 2.1.2, the Gaussian models are the analytical solution of a simplified advection-diffusion equation. In case of the G–BM model, the dispersion parameters were originally expressed as the product of the wind velocity's standard deviation multiplied by the travel time (Bultynck and Malet, 1972). It is interesting to note that this is the same expression Taylor obtained for the standard deviation of the particle positions for travel times smaller than the Lagrangian time scale (Taylor, 1922). In the G–BM model, this expression was used to calibrate the power law form of the dispersion parameters. Thus, since Taylor's theory is implicitly incorporated into the G–BM model, it might explain why its performance is situated between the open field models (LB–OF and LT–OF) and the LT–F model. Because the PG parameterization is obtained via direct calibration to tracer experiments, the effect of the autocorrelation is also likely incorporated implicitly. Incorporating the effect of the particle velocity's autocorrelation seems to enhance the consistency between models more strongly than the terrain parameterization does.

It should be remarked that a source strength measurement is not available for the SCK CEN site. Several source strength estimates are available and they differ within a factor of three. However, the correspondence between simulation results and observations is the best for the higher source strength Q_2. This is consistent with previous work from Pauly et al. (1997) in which good correspondence was obtained between the G–BM model and measured dose rates in the stations close to the stack and plume centerline for Q_2.

5. Conclusions

The performance of several dispersion models to predict dose rates in the first 300 m from the source on high-roughness terrain has been tested. Three types of models have been considered: the Gaussian model, the general advection-diffusion equation and the Langevin equation, each equipped with an open-field and forest terrain parameterization. It has been demonstrated that the vegetation canopy parameterization is capable of well predicting the wind profile inside the vegetation canopy. Also the capability of the open field and vegetation canopy parameterization to predict stratification has been validated by comparing with the in-house method. The distribution of the non-neutral records is consistently predicted between the vegetation canopy parameterization and the in-house method. The open field parameterization overpredicts the unstable conditions w.r.t. the in-house method. The three methodologies don't agree about the distribution of the neutral and near-neutral records. As a conclusion, the vegetation canopy parameterization gives reasonable results for high-roughness terrain.

An ambient gamma-dose-rate data set was obtained from routine Ar-41 releases originating from the BR1 reactor at the SCK CEN site, situated in a forest environment. Differences between the model performances are noticeable, where the Langevin equation with vegetation canopy parameterization tends to perform the best. Different values for the source strength have been reported, resulting in a rather high uncertainty on this parameter. The bias of the models remains always between a factor of one and four, partly due to the selected source strength. The uncertainty on the dose rates due to the model choice is a factor of 2.2 for a stack release, whereas this uncertainty for a ground releases is a factor of 14. The sensitivity analysis emphasizes that the wind direction is a sensitive parameter for dose-rate simulation that

should be carefully taken into account.

It should be emphasized that the dose-rate simulation can be extended to fluency rates by taking a weighted sum over the different nuclides. A recommendation for model improvement is to include a stochastically varying wind direction since the variation in wind direction has been demonstrated to be a sensitive parameter for dose rates in the near-field range. This effect becomes more dominant in low-wind speed conditions, such as occurring below the vegetation canopy. These might be topics for future research.

Declaration of competing interest

The authors declare that they have no known competing financial interests or personal relationships that could have appeared to influence the work reported in this paper.

Acknowledgment

A. Appendix: overview forest parameterization

Since the forest parameterization is quite extended, an overview is given here for the sake of convenience. The forest characteristics that need to be provided as an input are tree height (h), Leaf Area Density (LAD), Leaf Area Index (LAI), extinction coefficient (γ_{ext}) and drag coefficient (C_d). The requested meteorological parameters are the Von Kármán constant κ, pressure at ground level (p_0), air density at ground level (ρ), gravitational acceleration (g), measurement height z_{ref} of the wind speed $\overline{u}_{\text{ref}}$ above the canopy, measurement heights $\overline{z}_{\text{ref}}$ (above the canopy) and $z_{0,H}$ (between d and h) of the ambient temperatures leading to $\Delta\theta_{v,\text{ref}}$, the wind speed $\overline{u}_h$ located at h, the ambient temperature at h leading to $\Delta\theta_{v,0}$. It is not a requirement for the latter two measurements to be located at h, but they should at least be located in the roughness sublayer, i.e., between h and $Z_* + d$.

The next system needs to be solved for the parameters u_*, θ_*, L, μ_M and μ_H:

$$
\begin{cases}
\overline{u}(z_{\text{ref}} - d; u_*, \mu_M, L) &= \overline{u}_{\text{ref}} \\[4pt]
\overline{u}(h - d; u_*, \mu_M, L) &= \overline{u}_h \\[4pt]
L &= \dfrac{u_*^2 \theta_{v,0}}{\kappa g \theta_*} \\[4pt]
\theta_v\left(\overline{z}_{\text{ref}} - d; \theta_*, \mu_H, L\right) - \theta_{v,0} &= \Delta\theta_{v,\text{ref}} \\[4pt]
\theta_v(h - d; \theta_*, \mu_H, L) - \theta_{v,0} &= \Delta\theta_{v,0}
\end{cases}
\tag{A.1}
$$

If $\overline{u}_h$ and $\Delta\theta_{v,0}$ are not measured, then they can be estimated as $\overline{u}_h \approx \overline{u}_M(h - d; u_*, L)$ and $\Delta\theta_{v,0} \approx \theta_{v,M}(h - d; \theta_*, L) - \theta_{v,0}$. The MOST profiles together with the kernel functions and its integrated forms are as follows:

$$
\overline{u}(Z; u_*, \mu_M, L) = \frac{u_*}{\kappa}\left(\ln\left(\frac{Z}{z_0}\right) - \Psi_M(Z/L) \right.
$$
$$
\left. + \Psi_M(z_0/L) + \Psi_M^*\left(\frac{Z}{L}, \frac{Z}{Z_*}; \mu_M\right) - \Psi_M^*\left(\frac{z_0}{L}, \frac{z_0}{Z_*}; \mu_M\right) \right),
\tag{A.2}
$$

$$
\theta(Z; \theta_*, \mu_H, L) - \theta_{v,0} = \frac{\theta_*}{\kappa}\left(\ln\left(\frac{Z}{z_{0,H}}\right) - \Psi_H(Z/L) \right.
$$
$$
\left. + \Psi_H(z_{0,H}/L) + \Psi_H^*\left(\frac{Z}{L}, \frac{Z}{Z_*}; \mu_H\right) - \Psi_H^*\left(\frac{z_{0,H}}{L}, \frac{z_{0,H}}{Z_*}; \mu_H\right) \right),
\tag{A.3}
$$

$$
\Psi_i^*\left(\frac{Z}{L}, \frac{Z_*}{L}; \mu_i\right) \approx \Phi_i\left[\left(1 + \frac{1}{2\mu_i}\frac{Z_*}{Z}\right)\frac{Z}{L}\right] \frac{2}{3}\ln\left(1 + \frac{3}{2}\frac{Z_*}{\mu_i Z}\right)\exp(-\mu_i Z/Z_*), \quad i = M, H,
\tag{A.4}
$$

$$
\overline{u}_M(Z; u_*, L) = \frac{u_*}{\kappa\Gamma_1}\left(\ln\left(\frac{Z}{\alpha^2 z_0/\Gamma_1}\right) - \Psi_M(Z/L) + \Psi_M\left(\left[\alpha^2 z_0/\Gamma_1\right]/L\right) \right),
\tag{A.5}
$$

$$
\theta_M(Z; \theta_*, L) - \theta_{v,0} = \frac{\theta_*}{\kappa\Gamma_1}\left(\ln\left(\frac{Z}{\alpha^2 z_0/\Gamma_1}\right) - \Psi_H(Z/L) + \Psi_H\left(\left[\alpha^2 z_0/\Gamma_1\right]/L\right) \right),
\tag{A.6}
$$

$$
\Phi_H(Z/L) = \Phi_M^2(Z/L) = (1 - 16Z/L)^{-1/2}, \quad L < 0,
\tag{A.7}
$$

$$
\Phi_H(Z/L) = \Phi_M(Z/L) = 1 + 5Z/L, \quad L > 0,
\tag{A.8}
$$

$$
\Psi_H(Z/L) = 2\ln\left(\frac{1 + x^2}{2}\right), \quad x = (1 - 16Z/L)^{1/4}, \quad L < 0,
\tag{A.9}
$$

$$
\Psi_M(Z/L) = \ln\left[\left(\frac{1 + x^2}{2}\right)\left(\frac{1 + x}{2}\right)^2\right] - 2\arctan x + \frac{\pi}{2}, \quad x = (1 - 16Z/L)^{1/4}, L < 0,
\tag{A.10}
$$

$$
\Psi_M(Z/L) = \Psi_H(Z/L) = -5Z/L, \quad L > 0.
\tag{A.11}
$$

The ambient temperature T is converted to the virtual potential temperature θ_v as follows:

$$\theta_v(z) = T_v(z)\left(\frac{p_0}{p(z)}\right)^{R/c_p}, \quad R = 287\,\mathrm{J}/(\mathrm{kg\,K}), \quad c_p = 1004\,\mathrm{J}/(\mathrm{kg\,K}), \tag{A.12}$$

$$T_v(z) = T(z)\frac{1 + r_v(T(z))/0.622}{1 + r_v(T(z))}, \quad r_v(z) = \frac{0.622 e_v(T(z))}{p(z) - e_v(T(z))}, \quad e_v(z) = RH(z)e_s(T(z)), \tag{A.13}$$

$$p(z) = p_0 - \rho g z, \tag{A.14}$$

$$e_s(T) = \left[1.0007 + 3.46 \cdot 10^{-6} p_0\right] \cdot 611.21 \exp\left\{\frac{17.502 T}{240.97 + T}\right\}. \tag{A.15}$$

The parameters needed to evaluate the above functions correspond to:

$$d = \frac{\eta \alpha \overline{d}}{\eta(\alpha - 1) + 1}, \quad \overline{d} = \arg_z\max(\mathrm{LAD}(z)), \tag{A.16}$$

$$z_0 = 0.071 h, \tag{A.17}$$

$$Z_* = 2h - d, \tag{A.18}$$

$$\Gamma_1 = \eta(\alpha - 1) + 1, \quad \alpha^2 = 4(C_d \cdot \mathrm{LAI})^{1/2}, \quad \eta = 1 - \exp\{-\gamma_{\mathrm{ext}}\mathrm{LAI}\}, \tag{A.19}$$

$$\theta_{v,0} = \theta_v(z_{0,H}), \quad d + z_0 \leq z_{0,H} < h. \tag{A.20}$$

References

Adams, R., Essex, C., 2010. Calculus, a Complete Course, seventh ed. Pearson Canada, Toronto.

Arya, S.P., 2001. Introduction to Micrometeorology. In: Holton, J. (Ed.), International Geophysics Series, 2nd, vol. 79. Academic Press.

Blocken, B., Stathopoulos, T., Carmeliet, J., 2007. CFD simulation of the atmospheric boundary layer: wall function problems. Atmos. Environ. 41 (2), 238–252.

Briggs, G.A., 1982. Plume rise predictions. In: Lectures on Air Pollution and Environmental Impact Analyses. Springer, pp. 59–111.

Brisson, N., Seguin, B., Bertuzzi, P., 1992. Agrometeorological soil water balance for crop simulation models. Agric. For. Meteorol. 59 (3–4), 267–287.

Buck, A.L., 1981. New equations for computing vapor pressure and enhancement factor. J. Appl. Meteorol. 20 (12), 1527–1532.

Bultynck, H., Malet, L., 1972. Evaluation of atmospheric dilution factors for effluents diffused from an elevated continuous point source. Tellus 24 (5), 455–472.

Camps, J., 2018. The NERIS near-range atmospheric dispersion modelling experiment, 2018. Oral presentation given at the 4th NERIS Workshop, Dublin, Ireland. Presentation can be downloaded from. https://www.eu-neris.net/activities/worksho ps/dublin-2018.html (last checked on December 14, 2019).

Caughey, S.J., 1984. Observed characteristics of the atmospheric boundary layer. In: Atmospheric Turbulence and Air Pollution Modelling. Springer, pp. 107–158.

Chang, J.C., Hanna, S.R., 2004. Air quality model performance evaluation. Meteorol. Atmos. Phys. 87 (1–3), 167–196.

De Ridder, K., 2010. Bulk transfer relations for the roughness sublayer. Boundary-Layer Meteorol. 134 (2), 257–267.

De Visscher, A., 2013. Air Dispersion Modeling: Foundations and Applications. John Wiley & Sons.

Dyer, A.J., 1974. A review of flux-profile relationships. Boundary-Layer Meteorol. 7 (3), 363–372.

Gardiner, C.W., 1985. Handbook of Stochastic Methods for Physics, Chemistry and the Natural Sciences. In: Haken, H. (Ed.), Springer Series in Synergetics, 2nd, vol. 13. Springer-Verlag, Berlin.

Gielen, S., i Batlle, J.V., Vincke, C., Van Hees, M., Vandenhove, H., 2016. Concentrations and distributions of Al, Ca, Cl, K, Mg and Mn in a Scots pine forest in Belgium. Ecol. Model. 324, 1–10.

Gryning, S.-E., Batchvarova, E., Brümmer, B., Jørgensen, H., Larsen, S., 2007. On the extension of the wind profile over homogeneous terrain beyond the surface boundary layer. Boundary-Layer Meteorol. 124 (2), 251–268.

Hamby, D.M., 1994. A review of techniques for parameter sensitivity analysis of environmental models. Environ. Monit. Assess. 32 (2), 135–154.

Hanna, S.R., 1984. Applications in air pollution modeling. In: Atmospheric Turbulence and Air Pollution Modelling. Springer, pp. 275–310.

Holton, J.R., 2004. An Introduction to Dynamic Meteorology. In: Cynar, F. (Ed.), International Geophysics Series, 4th, vol. 88. Elsevier Academic Press.

Holtslag, A., 1984. Estimates of diabatic wind speed profiles from near-surface weather observations. Boundary-Layer Meteorol. 29 (3), 225–250.

Hunt, J., 1984. Diffusion in the stable boundary layer. In: Atmospheric Turbulence and Air Pollution Modelling. Springer, pp. 231–274.

Kenis, K., Vervecken, L., Camps, J., 2013. Gamma dose assessment in near-range atmospheric dispersion simulations. External Report of the Belgian Nuclear Research Centre; ER 242.

Kretzschmar, J., Mertens, I., Vanderborght, B., 1984. Development and Evaluation of the Possibilities of On-Line Dispersion Models for Use in an Emergency Plan of a Nuclear Installation. CEC Document XII. Technical report, SCK CEN.

Lamb, R.G., 1984. Diffusion in the convective boundary layer. In: Atmospheric Turbulence and Air Pollution Modelling. Springer, pp. 159–229.

Leelőssy, Á., Lagzi, I., Kovács, A., Mészáros, R., 2018. A review of numerical models to predict the atmospheric dispersion of radionuclides. J. Environ. Radioact. 182, 20–33.

Legg, B., Raupach, M., 1982. Markov-chain simulation of particle dispersion in inhomogeneous flows: the mean drift velocity induced by a gradient in Eulerian velocity variance. Boundary-Layer Meteorol. 24 (1), 3–13.

Lindroth, A., Perttu, K., 1981. Simple calculation of extinction coefficient of forest stands. Agric. Meteorol. 25, 97–110.

Mihailović, D., Lalić, B., Rajković, B., Arsenić, I., 1999. A roughness sublayer wind profile above a non-uniform surface. Boundary-Layer Meteorol. 93 (3), 425–451.

Mölder, M., Grelle, A., Lindroth, A., Halldin, S., 1999. Flux-profile relationships over a boreal forest–roughness sublayer corrections. Agric. For. Meteorol. 98, 645–658.

Mölder, M., Lindroth, A., 1999. Thermal roughness length of a boreal forest. Agric. For. Meteorol. 98, 659–670.

Oza, R., Daoo, V., Sitaraman, V., Krishnamoorthy, T., 1999. Plume gamma dose evaluation under non-homogeneous non-stationary meteorological conditions using particle trajectory model for short term releases. Radiat. Protect. Dosim. 82 (3), 201–206.

Pauly, J., Rojas-Palma, C., Sohier, A., 1997. Source Term Estimation Based on In-Situ Gamma Spectrometry Using a High Purity Germanium Detector. Centre de l'Etude de l'Energie Nucleaire. Technical report.

Porté, A., Bosc, A., Champion, I., Loustau, D., 2000. Estimating the foliage area of Maritime pine (Pinus pinaster Aït.) branches and crowns with application to modelling the foliage area distribution in the crown. Ann. For. Sci. 57 (1), 73–86.

Raupach, M., Thom, A.S., 1981. Turbulence in and above plant canopies. Annu. Rev. Fluid Mech. 13 (1), 97–129.

Raupach, M.R., Antonia, R.A., Rajagopalan, S., 1991. Rough-wall turbulent boundary layers. Appl. Mech. Rev. 44 (1), 1–25.

Raupach, M.R., Finnigan, J.J., Brunet, Y., 1996. Coherent eddies and turbulence in vegetation canopies: the mixing-layer analogy. Boundary-Layer Meteorol. 78 (3), 351–382.

Raza, S.S., Avila, R., Cervantes, J., 2001. A 3-D Lagrangian (Monte Carlo) method for direct plume gamma dose rate calculations. J. Nucl. Sci. Technol. 38 (4), 254–260.

Rojas-Palma, C., Aage, H.K., Astrup, P., Bargholz, K., Drews, M., Jørgensen, H.E., Korsbech, U., Lauritzen, B., Mikkelsen, T., Thykier-Nielsen, S., et al., 2004. Experimental evaluation of gamma fluence-rate predictions from Argon-41 releases to the atmosphere over a nuclear research reactor site. Radiat. Protect. Dosim. 108 (2), 161–168.

Sellier, D., Brunet, Y., Fourcaud, T., 2008. A numerical model of tree aerodynamic response to a turbulent airflow. Forestry 81 (3), 279–297.

Sonck, M., Desmedt, M., Claes, J., Sombre, L., Vandecasteele, C., 2010. TELERAD: the Radiological Surveillance Network and Early Warning System in Belgium. International Atomic Energy Agency (IAEA): IAEA. Technical report.

Srinivas, C., Venkatesan, R., Somayaji, K., Indira, R., 2009. A simulation study of short-range atmospheric dispersion for hypothetical air-borne effluent releases using different turbulent diffusion methods. Air Quality, Atmosphere & Health 2 (1), 21–28.

Stockie, J.M., 2011. The mathematics of atmospheric dispersion modeling. SIAM Rev. 53 (2), 349–372.

Stull, R.B., 1988. An Introduction to Boundary Layer Meteorology. In: Stull B., R. (Ed.), Atmospheric Sciences Library, 1st, vol. 13. Kluwer Academic Publishers, the Netherlands, Dordrecht.

Taylor, G.I., 1922. Diffusion by continuous movements. Proc. Lond. Math. Soc. s2–20 (1), 196–212.

Thom, A.S., 1971. Momentum absorption by vegetation. Q. J. R. Meteorol. Soc. 97 (414), 414–428.

Thykier-Nielsen, S., Deme, S., Láng, E., 1995. Calculation method for gamma dose rates from Gaussian puffs. RisøNational Laboratory 27 (3), 23.

Thykier-Nielsen, S., Deme, S., Mikkelsen, T., 1999. Description of the Atmospheric Dispersion Module RIMPUFF. Technical Report, Internal Report RODOS(WG2)-TN (98)-02.

Tubex, L., 2018. Een deeltjesmodel voor de dispersie van atmosferische releases op basis van meteorologische data met een hoge tijdsresolutie. Master's thesis. Antwerp University.

Vincke, C., 2006. Technical Report of the Post-doc Programme "Contribution to Long Term Biosphere Impact Modelling in a Geological Disposal Scenario through Measurements of Soil-Tree-Atmosphere Water Transfer and Related Ecophysiological Parameters". Technical Report. SCK CEN, p. 63p. Ref. I-90.

Vincke, C., Thiry, Y., 2008. Water table is a relevant source for water uptake by a Scots pine (Pinus sylvestris L.) stand: evidences from continuous evapotranspiration and water table monitoring. Agric. For. Meteorol. 148 (10), 1419–1432.

Vogel, S., 1984. Drag and flexibility in sessile organisms. Am. Zool. 24 (1), 37–44.

Wang, W., 2012. An analytical model for mean wind profiles in sparse canopies. Boundary-Layer Meteorol. 142 (3), 383–399.

Wieringa, J., 1992. Updating the Davenport roughness classification. J. Wind Eng. Ind. Aerod. 41 (1–3), 357–368.

Wilson, N.R., Shaw, R.H., 1977. A higher order closure model for canopy flow. J. Appl. Meteorol. 16 (11), 1197–1205.

Yi, C., 2008. Momentum transfer within canopies. Journal of Applied Meteorology and Climatology 47 (1), 262–275.

Zannetti, P., 1990. Air Pollution Modeling: Theories, Computational Methods and Available Software, 1st. Springer, US, New York.